Proceedings of the ECCOMAS Thematic International Conference on Simulation and Modeling of Biological Flows (SIMBIO 2011)
September 21–23, 2011, VUB, Brussels, Belgium

An Efficient Semi–Implicit Method for the Simulation of Blood Flow in Axially Symmetric Arteries.

Michael Dumbser [*], Vincenzo Casulli [*], and Eleuterio F. Toro [*]

1 Laboratory of Applied Mathematics
Via Mesiano, 77.
I-38100 Trento, Italy
michael.dumbser@ing.unitn.it

Abstract

Blood flow in arterial systems is described by the three-dimensional Navier-Stokes equations within a time dependent spatial domain that accounts for the viscoelasticity of the arterial walls. These equations are simplified by assuming cylindrical geometry, axially symmetric flow, and hydrostatic equilibrium in the radial direction. In this paper an efficient semi-implicit method is formulated in such a fashion that numerical stability is obtained at a minimal computational cost. The resulting computer model is relatively simple, robust, accurate, and extremely efficient. These features are illustrated on non trivial test cases where the exact analytical solution is known, and by an example of a realistic flow through a complex arterial system.
Keywords: blood flow; compliant arteries; moving boundaries; axially symmetric flow; hydrostatic equilibrium; semi-implicit method; finite difference; finite volume

Introduction

Blood flow in medium to large arterial systems can be accurately described by the three-dimensional *Navier-Stokes* equations within a time dependent spatial domain. These equations, however, are too complex to be efficiently solved over a network of systemic arteries and, alternatively, over-simplified one-dimensional equations are often used.

Assuming cylindrical geometry and axially symmetric flows, the two-dimensional Navier-Stokes equations in cylindrical coordinates can be considered to be a valid differential model for blood flow in compliant arteries. Moreover, since the axial scale is much larger than the radial scale, a dimensional analysis shows that the pressure can be assumed to be in (radial) hydrostatic equilibrium (see, *e.g.*, [1, 2]). Consequently, the *momentum* equation and the *incompressibility* condition for axially symmetric, hydrostatic flows in cylindrical coordinates are taken to be

$$\frac{\partial u}{\partial t} + u\frac{\partial u}{\partial x} + w\frac{\partial u}{\partial z} = -\frac{\partial p}{\partial x} + \frac{\nu}{z}\frac{\partial}{\partial z}\left(z\frac{\partial u}{\partial z}\right) \quad (1)$$

$$\frac{\partial (zu)}{\partial x} + \frac{\partial (zw)}{\partial z} = 0 \quad (2)$$

where $u(x,z,t)$ and $w(x,z,t)$ are the unknown velocity components in the axial x- and radial z-directions, respectively; t is the time; $p(x,t)$ is the normalized pressure, assumed to be in static equilibrium in the radial direction; and ν is a nonnegative kinematic viscosity coefficient.

The flow is confined within a dynamic boundary given by the arterial wall. Integrating the continuity equation along the radial direction, and using a kinematic condition at the moving boundary, leads to the following equation for the *moving vessel boundary*

$$\frac{\partial A}{\partial t} + 2\pi\frac{\partial}{\partial x}\left(\int_0^R zu\,dz\right) = 0 \quad (3)$$

where $A = \pi R^2$ is the cross section area and $R(x,t)$ is the unknown arterial radius.

To close the problem, an *equation of state*, relating the radius R to the unknown pressure p, needs to be specified. To this purpose, a typical choice is the law of Laplace

$$p = p_{ext} + \beta(R - R_0), \quad (4)$$

where p_{ext} is a specified external pressure, β is a positive *'rigidity coefficient'*, and R_0 is the equilibrium radius (see, e.g., [2]).

The boundary conditions at the arterial wall ($z = R$) and along the x-axis ($z = 0$), are assumed to be

$$u(x,R,t) = 0 \qquad \text{and} \qquad \left.\frac{\partial u(x,z,t)}{\partial z}\right|_{z=0} = 0 \quad (5)$$

1 A SEMI-IMPLICIT FINITE VOLUME MODEL

1.1 Unstructured staggered grid

To simulate arterial flows one assumes that the arterial system consists in a set of interconnected arterial branches where the flow is governed by equations (1)–(3). Each branch is then subdivided into an arbitrary set of non–overlapping segments so that the overall computational domain along the axial direction is composed by a total of N_s segments, having a non–uniform length $\Delta x_j,\ j = 1, 2, \ldots, N_s$. The left and the right end points of the j–th segment are identified by the indices $\ell(j)$ and $r(j)$, respectively.

Along the radial direction a finite difference mesh that allows up to N_z rings is defined by specifying a monotonically increasing radial distribution $z_{k+\frac{1}{2}},\ k = 0, 1, \ldots, N_z - 1$, with $z_{\frac{1}{2}} = 0$. By denoting with R_j^n the discrete arterial radius at the j–th axial location and time level t_n, the outer ring containing the moving vessel wall is denoted by K_j^n so that $K_j^n \leq N_z$ and $R_j^n - z_{K-\frac{1}{2}} > 0$. Moreover, in order to fully account for the dynamics of the moving boundary, a radial mesh distribution is locally defined as $z^n_{j,k+\frac{1}{2}} = z_{k+\frac{1}{2}}$ for all $k = 0, 1, \ldots, K_j^n - 1$ and $z^n_{j,K+\frac{1}{2}} = R_j^n$. Accordingly, the thickness of the k–th ring is given by $\Delta z^n_{j,k} = z^n_{j,k+\frac{1}{2}} - z^n_{j,k-\frac{1}{2}}$ and its mid radius is $z^n_{j,k} = \frac{1}{2}(z^n_{j,k+\frac{1}{2}} + z^n_{j,k-\frac{1}{2}})$ for all $k = 1, 2, \ldots, K_j^n$.

The discrete axial velocities $u^n_{j,k}$, assumed to be constant within each ring, are located at the center point of the j–th segment and for each radial location $k = 1, 2, \ldots, K_j^n$. The positive direction for $u^n_{j,k}$ is assumed to be from $\ell(j)$ to $r(j)$.

The discrete pressure p_i^n is located at the segment end points. The set of segments that share the i–th pressure point is denoted by $S_i,\ i = 1, 2, \ldots, N_p$, where N_p is the total number of pressure points. Typically, S_i contains two elements indicating the two consecutive segments within the same arterial branch that share the i–th pressure point. S_i contains only one element when the i–th pressure point is an end point of the arterial system, and S_i contains three or more elements when the i–th pressure point represents a junction of three or more arterial branches. When $j \in S_i$, then the i–th pressure point is an end point of the j–th segment, and $\wp(i, j)$ denotes the other end point of this segment, which is itself a pressure point and is a neighbor of the i–th pressure point. Finally, the discrete radial velocities $w^n_{i,k+\frac{1}{2}}$ are located on each pressure point and radially distributed at $z_{k+\frac{1}{2}}$ for all $k = 1, 2, \ldots, K_i^n - 1$.

1.2 Semi-implicit discretization

In order to derive a stable and efficient algorithm for simulating fluid flow in arterial systems, following some basic ideas commonly used in free-surface hydrodynamics [5, 8], the pressure in the momentum equation (1) and the velocity in the moving boundary equation (3), are discretized by the θ-method. In addition, for stability, the viscous term is discretized implicitly and the advective terms in equation (1) are discretized within an Eulerian-Lagrangian framework. Thus, a consistent *finite difference* discretization of the momentum equation, on each ring at the center of the j–th segment, is taken to be

$$\frac{u^{n+1}_{j,k} - u^{n,L}_{j,k}}{\Delta t} = -\frac{p^{n+\theta}_{r(j)} - p^{n+\theta}_{\ell(j)}}{\Delta x_j} + \nu \frac{z^n_{j,k+\frac{1}{2}} \frac{u^{n+1}_{j,k+1} - u^{n+1}_{j,k}}{\Delta z^n_{j,k+\frac{1}{2}}} - z^n_{j,k-\frac{1}{2}} \frac{u^{n+1}_{j,k} - u^{n+1}_{j,k-1}}{\Delta z^n_{j,k-\frac{1}{2}}}}{z^n_{j,k} \Delta z^n_{j,k}} \tag{6}$$

where Δt is the time step size; θ is an implicitness factor to be taken in the range $\frac{1}{2} \leq \theta \leq 1$ (see [5] for a detailed analysis of the θ-method); $p^{n+\theta} = \theta p^{n+1} + (1 - \theta)p^n$; $\Delta z^n_{j,k\pm\frac{1}{2}} = \frac{1}{2}(\Delta z^n_{j,k} + \Delta z^n_{j,k\pm1})$; and $u^{n,L}_{j,k}$ denotes the axial velocity component interpolated at time t_n at the end of the Lagrangian trajectory. The Lagrangian trajectory is calculated by integrating the velocity backwards in time from node (j, k) at t_{n+1} to its location at time t_n. Alternative explicit schemes for advection, such as a conservative formulation that allows for accurate simulation of rapidly varying flows [18], are also possible.

When $k = 1$ and $k = K_j^n$, respectively, the values of $u^{n+1}_{j,0}$ and $u^{n+1}_{j,K+1}$ in equation (6) are eliminated by means of the boundary conditions (5) which yield

$$u^{n+1}_{j,K+1} = -u^{n+1}_{j,K} \qquad \text{and} \qquad u^{n+1}_{j,0} = u^{n+1}_{j,1} \tag{7}$$

At each pressure point a semi-implicit *finite volume* approximation of the moving boundary equation (3) is taken to be

$$V_i(p_i^{n+1}) = V_i(p_i^n) - \Delta t \sum_{j \in S_i} \sigma_{i,j} \sum_{k=1}^{K_j^n} a^n_{j,k} u^{n+\theta}_{j,k} \tag{8}$$

where $a^n_{j,k} = 2\pi z^n_{j,k} \Delta z^n_{j,k}$ is the k–th cross section area, $u^{n+\theta}_{j,k} = \theta u^{n+1}_{j,k} + (1 - \theta)u^n_{j,k}$, and

$$V_i(p) = \frac{\pi}{2} \sum_{j \in S_i} \Delta x_j [R_j(p)]^2$$

is a nonlinear function representing the fluid volume associated with the i–th pressure point. As indicated, $V_i(p)$ is a function of the radii $R_j(p)$, for all $j \in S_i$ which, in turn, depend on the specified pressure p through the equation of state (4). Finally, $\sigma_{i,j}$ is a sign function associated with the orientation of the j–th axial velocity. Specifically,

$$\sigma_{i,j} = \frac{r(j) - 2i + \ell(j)}{r(j) - \ell(j)}$$

Equations (6) and (8) constitute a *mildly nonlinear* system of at most $N_z N_s + N_p$ equations. This system has to be solved at each time step in order to calculate the new field variables $u^{n+1}_{j,k}$ and p_i^{n+1} throughout the flow domain.

2 NUMERICAL TESTS

The above numerical method is first applied on two test problems with known analytical solution. Then a laminar boundary layer flow through a rigid tube at high Reynolds number is compared with reliable reference solutions available from boundary layer theory. Finally, the proposed algorithm is applied to simulate a pulsating flow through a simplified arterial system.

2.1 Steady flow in an elastic tube

In this test problem a steady flow through an elastic tube is numerically determined by applying the proposed algorithm over a sufficiently long time interval. For any given positive constants ν, β, p_{ext}, R_0 and Q, if the advective terms $u\frac{\partial u}{\partial x} + w\frac{\partial u}{\partial z}$ in the momentum equation (1) are neglected, an exact steady solution of problem (1)–(5) within the domain $\Omega = \{(x,z) : 0 \le x \le L; 0 \le z \le R(x)\}$, with $L < \frac{\pi\beta R_0^5}{40\nu Q}$, can be shown to be (see [10])

$$u(x,z) = \frac{2Q}{\pi R^4(x)}\left[R^2(x) - z^2\right] \tag{9}$$

$$p(x) = p_{ext} + \beta[R(x) - R_0] \tag{10}$$

where the tube radius is given by

$$R(x) = \sqrt[5]{R_0^5 - \frac{40\nu Q}{\pi\beta}x} \tag{11}$$

For the present test the chosen parameters are $\nu = 10^{-3}$, $\beta = 2500$, $p_{ext} = 0$, $R_0 = 0.025$, $Q = 0.001875$ and $L = 1$. Numerically, a transient solution is generated from the starting time $t = 0$ with initial conditions $u(x,z,0) = 0$ and $R(x,0) = R_0$. Then, for times $t > 0$, the boundary conditions at the inlet ($x = 0$) are given by specifying the exact velocity profile from equation (9), and the exact pressure at the outlet ($x = L$) is prescribed according to equation (10).

The computational domain is discretized with $N_s = 100$ segments in the axial direction, and $N_z = 50$ rings are used along the radial direction to discretize the reference radius R_0. Assuming that the steady state is reached at the final time $t_e = 10$, by using $\theta = 1$ the simulation is advanced for $N_t = 100$ time steps with a time step size $\Delta t = t_e/N_t$. The resulting tube radius obtained at $t = t_e$, and some representative velocity profiles at different axial locations, are illustrated in Figure 1. The classical parabolic Hagen–Poiseuille profile for the velocity is well reproduced and an overall excellent agreement between the numerical results and the exact solution is clearly shown.

Since the analytical solution of the present test problem is sufficiently smooth, the order of accuracy of the proposed algorithm can be numerically determined by successively refining the spatial grid size. To this purpose, the discrete L_2 error norms for the axial velocity and for the radius, respectively, are taken to be

Table 1: Numerical convergence results in L_2 error norm for $u(x,z)$ and for $R(x)$

N_p	N_z	$\epsilon_{L_2}^{u,N_t}$	$\mathcal{O}_{L_2}^u$	$\epsilon_{L_2}^{R,N_t}$	$\mathcal{O}_{L_2}^R$
100	50	2.9227E-05		4.1649E-06	
200	100	7.5484E-06	2.0	1.1241E-06	1.9
400	200	1.9181E-06	2.0	2.9256E-07	1.9
800	400	4.8321E-07	2.0	7.4158E-08	2.0

$$\epsilon_{L_2}^{u,n} = \sqrt{2\pi \sum_{j=1}^{N_s}\sum_{k=1}^{K_j^n}\left[u_{j,k}^n - u(x_j, z_k^n)\right]^2 z_k^n \Delta x_j \Delta z_{j,k}^n} \tag{12}$$

$$\epsilon_{L_2}^{R,n} = \sqrt{\sum_{j=1}^{N_s}\left[R_j^n - R(x_j)\right]^2 \Delta x_j} \tag{13}$$

where the exact solution for $u(x_j, z_k^n)$ and $R(x_j)$ is given by equations (9) and (11), respectively. The errors $\epsilon_{L_2}^{u,n}$ and $\epsilon_{L_2}^{R,n}$ are computed by using a sequence of successively refined meshes obtained with $N_s = 100$, 200, 400 and 800, and $N_z = 50$, 100, 200 and 400, respectively. The time step size is kept constant $\Delta t = 0.1$. The convergence results listed in Table 1 indicate that the designed second order of accuracy, $\mathcal{O}_{L_2}^u$ and $\mathcal{O}_{L_2}^R$, is achieved for this steady test problem.

2.2 Womersley profiles

In this section the proposed semi–implicit scheme is verified against the exact solution found by Womersley for an oscillating flow in a rigid tube [19]. The flow is driven by a sinusoidal pressure gradient (pressure difference)

$$\frac{p_{\text{out}}(t) - p_{\text{in}}(t)}{L} = -\frac{\hat{P}}{\rho}\, e^{i\omega t} \tag{14}$$

which is imposed at the ends of a tube of length L. Here, $\hat{P}$ is the amplitude of the oscillating pressure gradient, ρ is the fluid density, p_{in} is the pressure at the tube inlet, p_{out} is the pressure on the tube outlet, ω is the angular frequency and $i = \sqrt{-1}$ denotes the imaginary unit. According to Womersley [19], the axial velocity profile is uniform in the x direction and is given by the real part of the expression

$$u(x,z,t) = \frac{\hat{P}}{\rho}\frac{1}{i\omega}\left[1 - \frac{J_0(\alpha y i^{\frac{3}{2}})}{J_0(\alpha i^{\frac{3}{2}})}\right] e^{i\omega t} \tag{15}$$

with

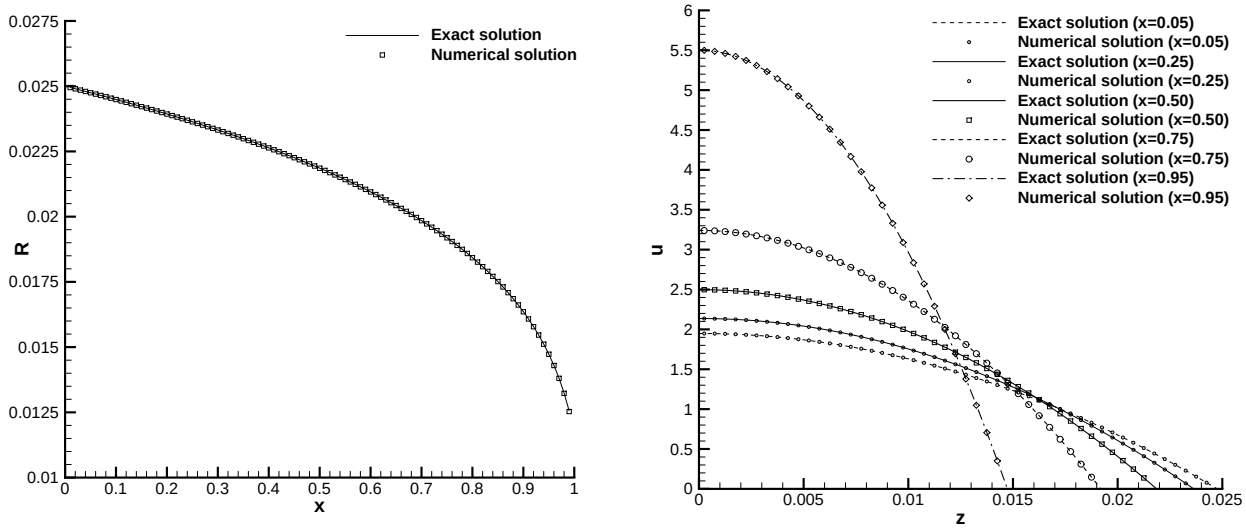

Figure 1: Comparison of the numerical results obtained at time $t_e = 10.0$ with the exact steady solution. Shape of the elastic tube (left) and selected velocity profiles at different axial positions (right).

$$y = \frac{z}{R} \qquad \text{and} \qquad \alpha = R\sqrt{\frac{\omega}{\nu}}$$

Here, J_0 is the zero–th order Bessel function of the first kind, and y is the dimensionless radial coordinate. For the present test the chosen parameters are $L = 1$, $R = 0.025$, $\hat{P} = 1000$, $\rho = 1000$, $\omega = 2\pi$ and $\beta = 10^{12}$ so that the tube wall is sufficiently rigid. Moreover, in order to match the Womersley solution, the nonlinear advective terms are neglected.

For the viscosity two cases are considered. In a first case a low Reynolds number (that is based on the tube diameter $D = 2R = 0.05$) is obtained by choosing $\nu = 10^{-3}$. In this case $Re = 50$, the resulting viscous effect dominates the entire tube, and the velocity profile resembles the classical Hagen–Poiseuille flow. In a second case, by choosing $\nu = 10^{-5}$ the corresponding Reynolds number is $Re = 5000$ and the resulting viscous effect is essentially confined to a boundary layer close to the tube wall. In this case the velocity profile is essentially flat at the center of the tube, whereas a sharp boundary–layer with high velocity gradients develops near the tube walls.

As initial conditions, $u(x, z, 0)$ is taken from equation (15), and $R(x, 0) = R_0$ is assumed. Then, for times $t > 0$ the analytic pressure gradient from (14) is specified at the two ends of the tube as boundary conditions.

The computational domain is then discretized with $N_s = 100$ segments in the axial direction and $N_z = 50$ rings in radial direction. By using $\theta = 0.5$ and a fixed time–step size $\Delta t = 0.01$, the unsteady simulation covers three cycles until a final time $t_e = 3$ is reached. The computated results for both, the low and the high Reynolds number case, are illustrated in Figure 2. An excellent agreement between the numerical and the exact solution is clearly shown. Note, in particular, that only a few grid points are sufficient to resolve the sharp boundary layer in the high Reynolds number case. This aspect turns out to be quite useful in realistic simulations of cardio–vascular circulation, where the Reynolds number changes over several orders of magnitude from the big vessels down to the capillaries.

Table 2: Numerical convergence results in L_2 error norm for the axial velocity at time $t_e = 2.0$.

N_s	N_z	N_t	$\epsilon^u_{L_2}$	$\mathcal{O}^u_{L_2}$
400	100	100	5.2651E-06	
800	200	200	1.5000E-06	1.8
1600	400	400	3.9949E-07	1.9
3200	800	800	1.0319E-07	2.0

The model accuracy for the present *unsteady* test problem is established numerically by measuring the error norm on a series of simulations obtained with successively refined meshes. Moreover, in order to verify the time accuracy, the time step size is reduced accordingly. Thus, with reference to the high Reynolds number flow ($Re = 5000$), the error norm $\epsilon^u_{L_2}$ is computed at $t_e = 2$ by using a sequence of successively refined meshes with $N_s = 400$, 800, 1600, 3200; $N_z = 100$, 200, 400, 800; and $N_t = 100$, 200, 400, 800, respectively. For this test the θ-method with $\theta = 0.5$ is extended also to the viscous term.

The convergence results are listed in Table 2, where the L_2–error norm $\epsilon^u_{L_2}$ and the resulting order of accuracy $\mathcal{O}^u_{L_2}$ are reported to confirm that second order of accuracy is achieved also for solving *unsteady* flow problems.

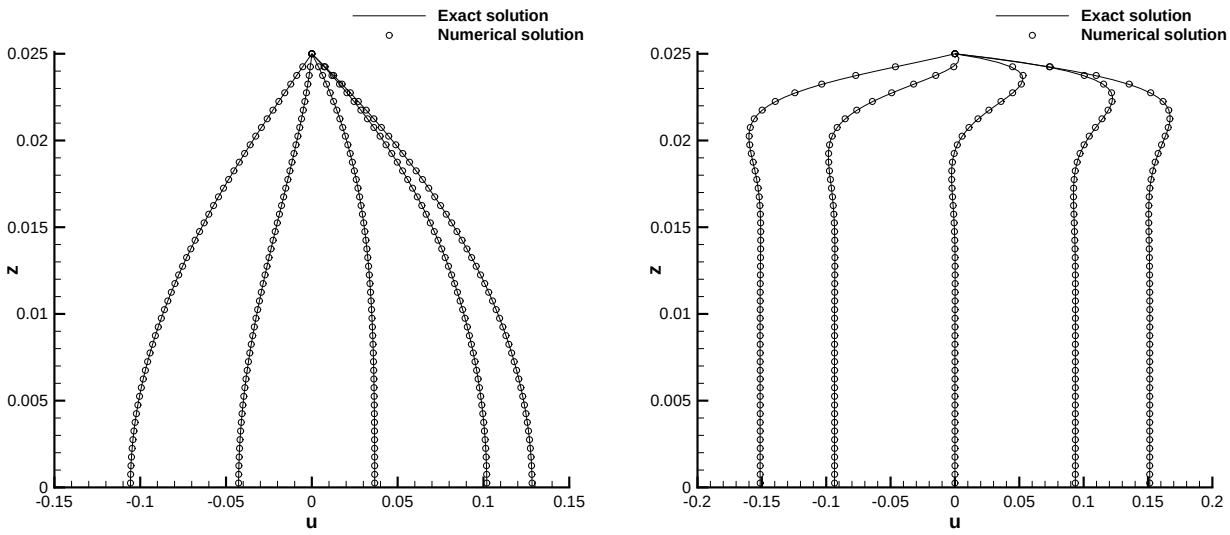

Figure 2: Comparison of the exact solution of Womersley [19] with the numerical results at different times. Left ($Re = 50$): the different graphs from left to right correspond to the times $t = 1.7$, $t = 1.8$, $t = 1.9$, $t = 2.0$ and $t = 2.1$, respectively. Right ($Re = 5000$): the different graphs from left to right correspond to the times $t = 1.8$, $t = 1.9$, $t = 2.0$, $t = 2.1$ and $t = 2.2$, respectively.

2.3 Laminar high Reynolds number boundary layer

The test problem presented in this section is motivated from the pure necessity of a thorough code validation rather than from the physics of real physiological flows. In all the previous test problems, the nonlinear convective terms could be neglected, hence in this section a test problem with known reference solution is considered where the convective terms are important. For this purpose, a steady high Reynolds number boundary layer flow in a rigid tube of length L with variable cross section is considered. In the present test the nonlinear advective terms play a crucial role and cannot be neglected because, according to the classical boundary layer theory of Prandtl [14, 15], the convective accelerations within the boundary layer are of order 1 in axial direction, whereas the vertical accelerations are of the same order of the boundary layer thickness. It is well known [15] that in tubes with *constant* radius, boundary layers produce a displacement effect, which causes an acceleration of the fluid in the inviscid core of the flow. Therefore, in order to preserve a uniform axial velocity within the inviscid inner core of the tube, an appropriate (non constant) tube radius must be selected. This is achieved by taking

$$R(x) = R_0 + \delta(x) \tag{16}$$

where R_0 is the radius at the tube inlet at $x = 0$ and $\delta(x)$ is the displacement thickness of the boundary layer. For sufficiently high Reynolds numbers the boundary layer is so thin that it behaves like the boundary layer on a flat plate, see [13] and [15]. The classical Blasius boundary layer solution on a flat plate is given by

$$u(x, y) = U_0 f'(\eta), \qquad \text{with} \qquad \eta = y\sqrt{\frac{U_0}{2\nu x}}$$

where $y = R - z$ is the distance from the tube wall, η is the dimensionless wall distance and U_0 is the inflow velocity. The function $f(\eta)$ is the solution of the classical Blasius boundary layer equation

$$f''' + f f' = 0 \tag{17}$$

with the usual boundary conditions

$$f(0) = 0, \quad f'(0) = 0, \quad \lim_{\eta\to\infty} f'(\eta) = 1 \tag{18}$$

where the primes denote derivatives with respect to η. In the present investigation $f(\eta)$ is determined by solving the boundary value problem (17)-(18) with a tenth order discontinuous Galerkin finite element scheme described in [9]. The displacement thickness of the Blasius boundary layer needed in equation (16) is then given by

$$\delta(x) = \sqrt{\frac{2\nu x}{U_0}} \int_0^\infty [1 - f'(\eta)] d\eta$$

For the present test the chosen parameters are $L = 1$, $R_0 = 0.1$, $U_0 = 1$, $\beta = 10^{12}$, and $\nu = 10^{-6}$, which corresponds to a Reynolds number $Re = 200,000$ based on the inflow velocity U_0 and the inlet tube diameter $2R_0$. Numerically, a transient solution is generated from the starting time $t = 0$ with initial conditions $u(x, z, 0) = U_0$ and

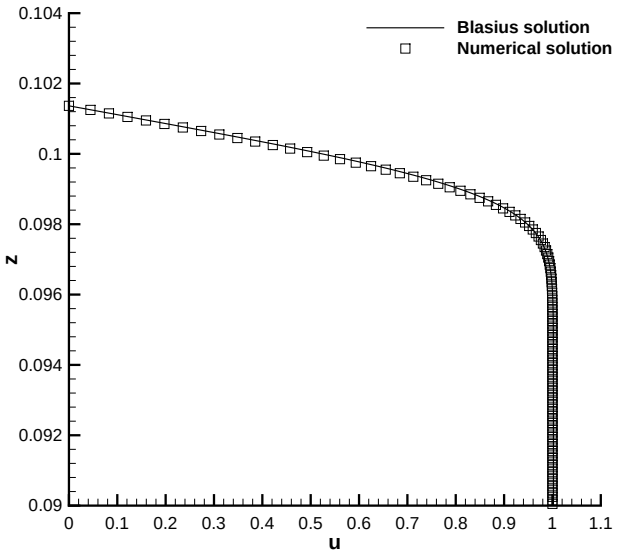

Figure 3: Comparison of the Blasius boundary layer solution with the numerical results.

$R(x)$ given by equation (16). Then, for times $t > 0$, at the inlet ($x = 0$) a constant velocity $u(0, z, t) = U_0$ is imposed as a boundary condition, and at the outlet ($x = L$) a pressure boundary condition $p(L, t) = 0$ is prescribed.

The chosen grid is uniform with $N_s = 100$ segments along the axial direction, and has a non–uniform distribution of $N_z = 168$ rings in radial direction with a spacing of $\Delta z^n_{j,k} = 5 \cdot 10^{-3}$ for $z \in [0; 0.085]$ and $\Delta z^n_{j,k} = 10^{-4}$ for $z > 0.085$. Assuming that the steady state is reached at the final time $t_e = 5$, by using $\theta = 1$ the simulation is advanced for $N_t = 50$ time steps with a time step size $\Delta t = t_e/N_t$. In Figure 3 the numerical results are compared at the axial position $x = 0.75$ with the Blasius boundary layer solution. An excellent agreement between the two solutions can be observed. Moreover, because of the radius adjustment, the inviscid core of the flow maintains the prescribed inflow velocity $U_0 = 1$ with good accuracy.

2.4 Application to a realistic model of the human arterial system

Simulating blood flow in large systemic arteries is a challenging task usually tackled by one-dimensional models (see, e.g., [12, 16, 17]). In the present test a simplified but realistic human arterial system is considered. Here, advection, viscosity and wall elasticity are equally important. This system contains 55 branches with varying lengths, rigidity coefficients, and equilibrium radii, as detailed in [16]. A sketch of the system is shown in Figure 4. The overall system length is $7.341\,m$ where the blood is assumed to be a Newtonian fluid with constant viscosity $\nu = 4.0 \cdot 10^{-6}$, according to [13].

Numerically, a periodic solution is generated from the starting time $t = 0$ with initial conditions $u(x, z, 0) = 0$ and $p(x, 0) = p_{ext}$, where the equilibrium reference pressure is $p_{ext} = 80\,mmHg$, ($1\,mmHg = 133.322\,Pa$). Then, for times $t > 0$, the boundary condition at the ascending aorta is prescribed by specifying a periodic pressure signal with period $T = 1\,s$, similar to the waveform used in [16]. Specifically,

$$p_{\text{in}}(t) = \frac{\hat{P}}{\rho K} \max[0, \sin(2\pi t + 0.628) - 0.588] \quad (19)$$

where $\hat{P} = 40\,mmHg$ is the maximum amplitude of the pressure wave, $\rho = 1000\,kg/m^3$ is the fluid density, and $K = 0.412$ is a normalization constant. On the remaining 28 open ends of the arterial tree, transmissive boundary conditions are imposed.

The arterial system is decomposed into a set of segments with an almost uniform length $\Delta x_j = 5\,mm$ resulting into $N_p = 1,448$ pressure points. Then, assuming that the arterial radius does not exceed the value $R_0 = 2\,cm$, by choosing $N_z = 100$ one has a uniform radial mesh spacing $\Delta z_k = 0.2\,mm$. The simulation covers 10 cardiac cycles until $t_e = 10\,s$ with $\theta = 0.6$ and $N_t = 1,000$, so that the time step size is $\Delta t = 0.01\,s$. It is important to recall that nonlinear advective terms have been discretized by using the Eulerian–Lagrangian approach. Consequently, for any $\theta \geq \frac{1}{2}$ the proposed method can be shown to be unconditionally stable [5], but the time step size has to be small enough merely to resolve this short time scale.

The resulting time histories for pressure, artery radius and axial velocity at $z = 0$ are shown in Figure 5 at four different locations, namely at the end of the ascending aorta, at the end of the right carotid, at the end of the right subclavian and at the end of the right femoral artery (the precise locations are highlighted in Figure 4). Figure 6 shows some detailed velocity profiles calculated at the above locations. It can be seen that the velocity profile in the ascending aorta is almost flat, due to the high Reynolds number at this location, whereas the reduced Reynolds number in the smaller arteries yields velocity profiles that are similar to the classical parabolic Hagen–Poiseuille flow.

To validate the above results, the previous calculations are systematically repeated with all parameters unchanged, except radial resolution that starts with $N_z = 1$ (which corresponds to a one–dimensional, sectionally averaged model) and goes up to $N_z = 10$, 100, 1000, and 10000. The latter mesh has $N_p N_z = 14,480,000$ control volumes and an extremely fine radial mesh size $\Delta z_k = 2\,\mu m$. For each mesh resolution Figure 7 (left) shows the cross section average velocity computed at the end of the ascending aorta during the tenth cardiac cycle. A general good agreement can be observed and, in particular, convergence is indicated by the velocity signals obtained with $N_z = 100$, 1000 and 10000 that practically overlap. Hence $N_z = 100$ used earlier, can be assumed to provide a sufficiently detailed radial resolution. Moreover, the computed waveform, as well as the wave amplitudes are in good agree-

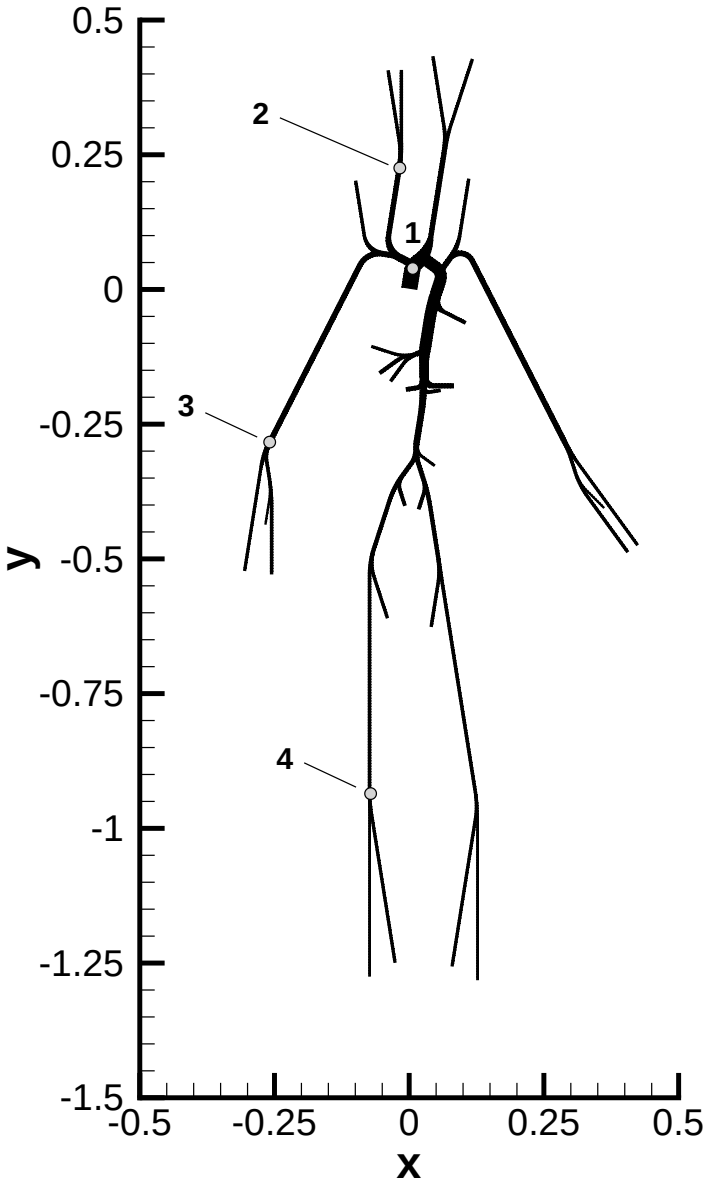

Figure 4: Sketch of the topology of the 55 arteries considered in the model application. The ascending aorta (1), the right carotid (2), the right subclavian and the right femoral artery (4) are highlighted.

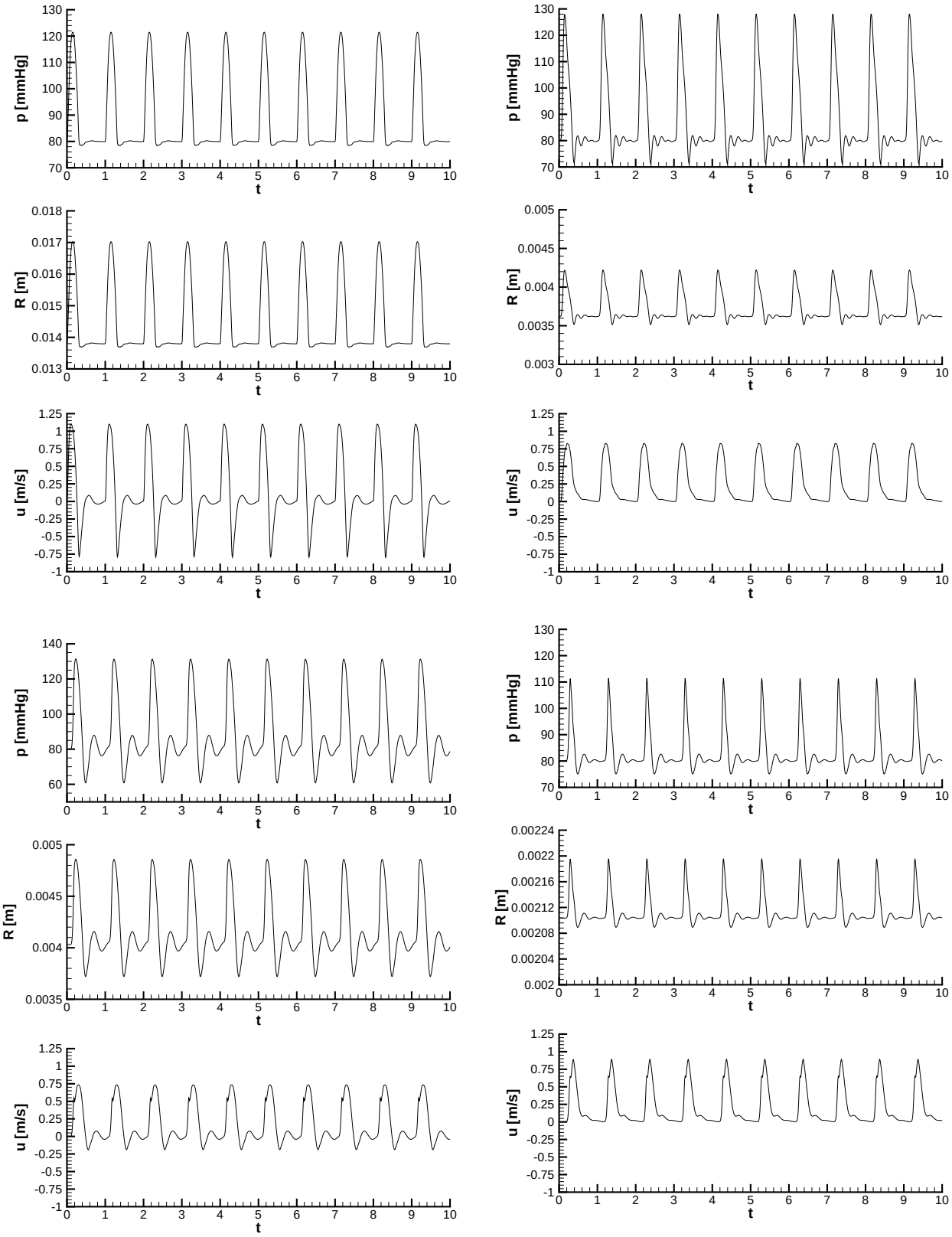

Figure 5: Time histories of pressure, radius, and axial velocity at $z = 0$ in the ascending aorta (top left), in the right carotid (top right), in the right subclavian (bottom left) and in the right femoral artery (bottom right).

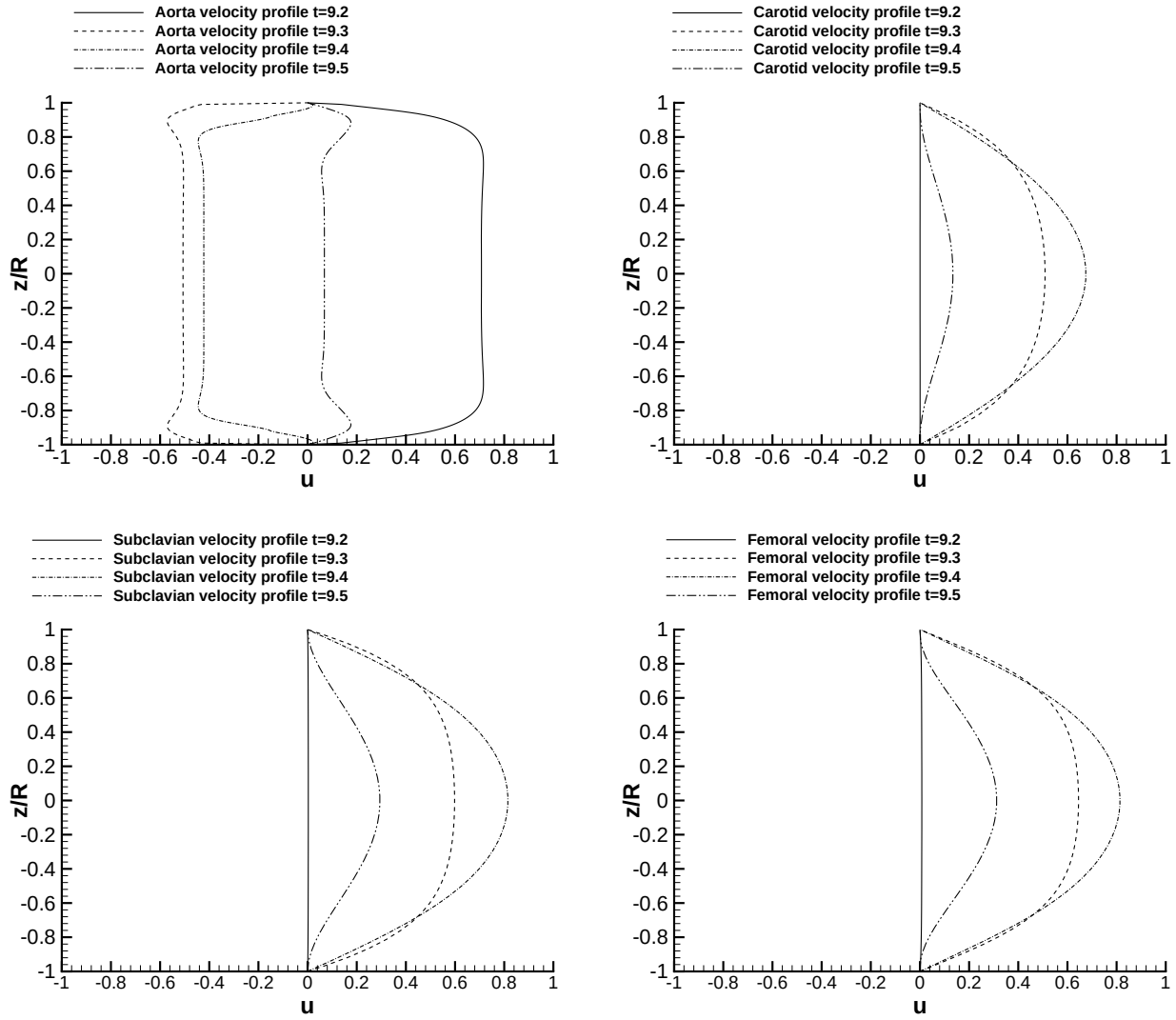

Figure 6: Selected velocity profiles during the tenth cardiac cycle in the ascending aorta (top left), in the right carotid (top right), in the right subclavian (bottom left) and in the right femoral artery (bottom right).

ment with the experimental results presented in [11]. For comparison, the simplified waveform of the experimental results reported in [13] is shown on the right of Figure 7.

The above calculations have been performed on a laptop with an Intel $i7$ CPU having $2.80\,GHz$ clock frequency and $6\,GB$ of RAM. The problem size and the required computer time to complete one cardiac cycle for different radial resolution are reported in Table 3. These results confirm that the proposed numerical method is very accurate, highly efficient and a good candidate for large–scale simulations of the human cardio–vascular system.

Conclusions

A semi-implicit method for solving the governing equations of axially symmetric, hydrostatic flows in cylindrical coordinates has been presented. The combination of judicious selection of terms that are discretized implicitly and use of an Eulerian-Lagrangian method for treating the advective terms makes the present formulation stable, simple and extremely efficient. The resulting method is locally and globally mass conservative. The computed results for different test problems verify the computational performance and the accuracy of the proposed algorithm. This model can potentially be used as one of the elements in future interdisciplinary investigations at large scale, considering a much more detailed model for the human cardio–vascular system than the simplified test problem studied in this paper. The method may also provide the basic hydrodynamic information needed for the simulation of transport processes, e.g. in the context of drug–delivery.

Acknowledgements

This work was in parts co–financed by the *Deutsche Forschungsgemeinschaft* (DFG) under the *Heinz Maier–Leibnitz* programme 2007.

References

[1] Barnard, A.C.L., W.A. Hunt, W.P. Timlake, and E.Varley, 'A theory of fluid flow in compliant tubes', *Biophysical Journal* 1966; **6**:717–724.

[2] S. Čanić, C.J. Hartley, D. Rosenstrauch, J. Tambača, G. Guidoboni, and A. Mikelič, 'Blood flow in compliant arteries: An effective viscoelastic reduced model, numerics, and experimental validation', *Annals of Biomedical Engineering* 2006; **34**:575–592.

[3] V. Casulli, 'Semi-implicit finite difference methods for the two-dimensional shallow water equations', *J. Comput. Phys.* 1990; **86**:56–74.

[4] V. Casulli and R.T. Cheng, 'Semi-implicit finite difference methods for three-dimensional shallow water flow', *Int. J. Numer. Meth. Fluids*. 1992; **15**:629–648.

[5] V. Casulli and E. Cattani, 'Stability, accuracy and efficiency of a semi-implicit method for three-dimensional shallow water flow', *Comput. Math. Appl*. 1994; **27**:99–112.

[6] V. Casulli and R.A. Walters, 'An unstructured grid, three-dimensional model based on the shallow water equations', *Int. J. Numer. Meth. Fluids*. 2000; **32**:331–348.

[7] V. Casulli, 'A high-resolution wetting and drying algorithm for free-surface hydrodynamics', *Int. J. Numer. Meth. Fluids*. 2009; **60**:391–408.

[8] V. Casulli and G.S. Stelling, 'Semi-implicit subgrid modelling of three-dimensional free-surface flows', *Int. Jour. for Numerical Methods in Fluids*. 2011; DOI: 10.1002/fld.2361.

[9] M. Dumbser, 'Arbitrary high order PNPM schemes on unstructured meshes for the compressible Navier–Stokes equations', *Computers & Fluids*. 2010; **39**:60–76.

[10] Y.C. Fung, *Biomechanics: Circulation*. Second edition. Springer New York, Berlin, Heidelberg, 2010.

[11] R.M. Nerem, W.A. Seed and N.B. Wood., 'An experimental study of the velocity distribution and transition to turbulence in the aorta', *J. Fluid Mech.*. 1972; **52**:137–160.

[12] M.S. Olufsen, C.S. Peskin, W.Y. Kim, E.M. Pedersen, A. Nadim, and J. Larsen, 'Numerical simulation and experimental validation of blood flow in arteries with structured-tree outflow conditions', *Annals of Biomedical Engineering* 2000; **28**:1281–1299.

[13] T.J. Pedley, *The fluid mechanics of large blood vessels*. Cambridge University Press, Cambridge, 1980.

[14] L. Prandtl. Über Flüssigkeitsbewegung bei sehr kleiner Reibung. *Verhandlg. III. Intern. Math. Kongr. Heidelberg*, pages 484–491, 1904.

[15] H. Schlichting and K. Gersten, *Boundary–Layer Theory*. Springer, Berlin, 1999.

[16] S.J. Sherwin, L. Formaggia, J. Peiró and V. Franke, 'Computational modelling of 1D blood flow with variable mechanical properties and its application to the simulation of wave propagation in the human arterial system', *Int. J. Numer. Meth. Fluids*. 2003; **43**:673–700.

[17] S.J. Sherwin, V. Franke, J. Peiró and K. Parker, 'One-dimensional modelling of a vascular network in space-time variables', *Journal of Engineering Mathematics*. 2003; **47**:217–250.

[18] G.S. Stelling and S.P.A. Duynmeyer, 'A staggered conservative scheme for every Froude number in rapidly varied shallow water flows', *Int. J. Numer. Meth. Fluids*. 2003; **43**:1329–1354.

[19] J.R. Womersley, 'Method for the calculation of velocity, rate of flow and viscous drag in arteries when the pressure gradient is known', *Journal of Physiology*. 1955; **127**:553–563.

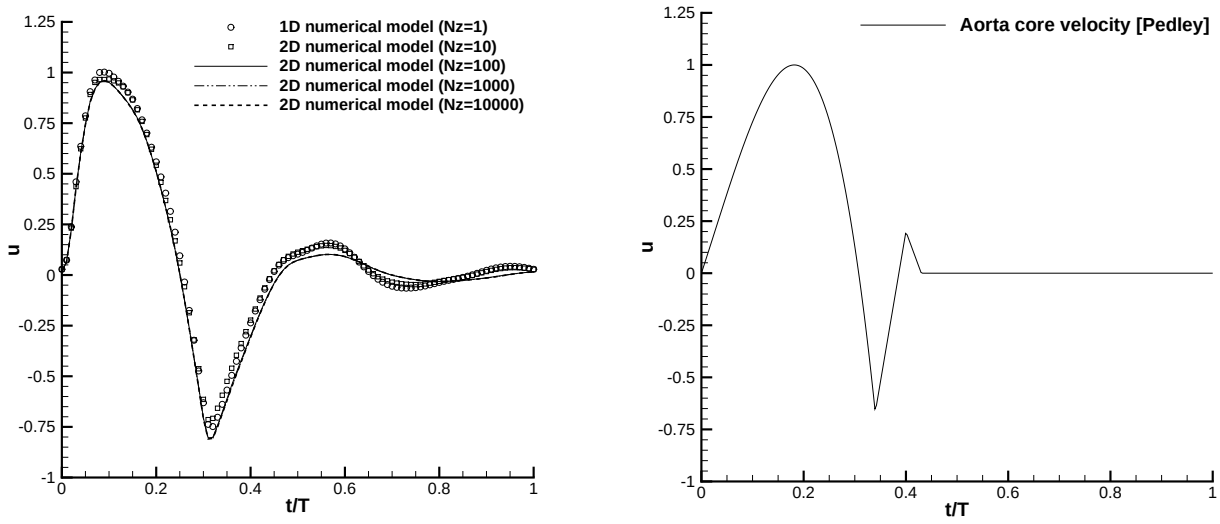

Figure 7: Left: Velocity signals in the ascending aorta computed during the tenth cardiac with varying radial resolution. Right: Simplified experimental waveform according to Pedley [13].

Table 3: Model size and wallclock time needed for the simulation of one cardiac cycle

Radial resolution	Number of control volumes ($N_p N_z$)	Computer time
$N_z = 1$ (1D model)	1,448	0.35 s
$N_z = 10$ (2D model)	14,480	0.38 s
$N_z = 100$ (2D model)	144,800	1.40 s
$N_z = 1,000$ (2D model)	1,448,000	13.14 s
$N_z = 10,000$ (2D model)	14,480,000	278.00 s